# Structural and electrical studies of nano structured $Sn_{1-x}Sb_xO_2$ ($x$ = 0.0, 1, 2.5, 4.5 and 7 at%) prepared by co-precipitation method

**V. Senthilkumar · P. Vickraman · M. Jayachandran · C. Sanjeeviraja**

**Abstract** $SnO_2$ semiconducting nanopowders doped with antimony $Sn_{1-x}Sb_xO_2$ ($x$ = 0.0, 1, 2.5, 4.5 and 7 at%) was achieved by co-precipitation method. TG/DTA and FT-IR studies revealed the removal of organic residuals in the precursor leading to the formation of oxides during calcinations process. A change in color from white to bluish occurred on calcinations of the powder at 500 °C in air. The distortion ratio, strain and particle size were measured from X-ray diffraction (XRD) spectra and their changes with dopants concentration were determined. Transmission electron microscopy (TEM) images support to conform the particle size. The electrical resistivity and activation energy of the ATO particles decreases as compared with pure $SnO_2$, due to the incorporation of on $Sn^{4+}$ ions by as $Sb^{5+}$ ion in the host $SnO_2$ matrix. Incorporation of $Sb^{5+}$ was evidenced through the XPS spectrum.

## 1 Introduction

Transparent conducting oxides (TCOs) are unique group of materials that offer both low resistivity and high transmissivity in the visible region. Common TCO materials include donor-doped oxides such as $SnO_2$, $In_2O_3$, ZnO and their ternary alloys with tin doped indium oxide (ITO) are being the most widely used TCO materials [1–4]. Due to heavy demand of supply, high expensiveness of indium and the difficulty of etching indium based TCOs by wet chemical methods during the patterning process; research has drifted to $SnO_2$-based $TCO_S$. One of the notable properties of SnO2 is its wide band gap (3.6 eV), and its conducting is generally caused by nonstoichiometry associated with oxygen vacancies available in the $SnO_2$ lattice [5]. The range of conductivity is found to be limited to $10^2$–$10^3$ $\Omega^{-1}$ cm$^{-1}$ which is unstable during its operation due to the interaction of oxygen vacancies with ambient oxygen [6–9].

Doping $SnO_2$ with proper elements, such as Sb, F and Mo is often available for applications in various areas such as displays, electrochromic windows, gas sensors, catalysts, rechargeable Li batteries, and optical electronic devices [10, 11]. Specially, Sb is the best dopant, because $SnO_2$ is of the preferable conductivity and transparency in visible light wavelength range after it is doped with antimony. Sb-doped $SnO_2$ (ATO) nanoparticles are usually synthesized by means of a variety of techniques, for example; hydrothermal [5], combustion [12], Sol–gel [13], micro emulsions [14], solid state reaction [15] Pechini method [15] and co-precipitation [16].

Especially, co-precipitation process has been used in many fields of advanced ceramics because the product purity and homogeneity have the possibility to control the physical properties and particle shapes. On the other hand, the route is operated easily and requires few expensive apparatuses and instruments.

In this paper, the synthesis of antimony doped $SnO_2$ nanoparticles via the Co-precipitation method from the

V. Senthilkumar · P. Vickraman (✉)
Department of Physics, Gandhigram Rural University,
Gandhigram 624302, India
e-mail: vrsvickraman@yahoo.com

V. Senthilkumar
e-mail: senthilvelu78@yahoo.com

M. Jayachandran
Electrochemical Material Science Division,
Central Electrochemical Research Institute, Karaikudi, India

C. Sanjeeviraja
Department of Physics, Alagappa University, Karaikudi, India

antimony(III) chloride and tin(II) chloride dihydrate is reported.

## 2 Experimental procedure

The antimony doped tin oxide nanocrystalline powders were prepared by co-precipitation method. The starting solution of high purity $SnCl_2·2H_2O$ (analytical reagent) and antimony chloride with different atomic weight ratios $Sn_{1-x}Sb_xO_2$ ($x = 0.0, 1, 2.5, 4.5$ and $7$ at%) were prepared. The starting chemicals of Tin chloride and appropriate amount of $SbCl_3$ were dissolved in 500 ml of distilled water. This mixed solution was slowly added to the solution of 25 ml of acetylacetone in 70 ml of methanol by rapid stirring .The added acetylacetone took about 45 min, for its complete dissolution even with constant rapid stirring. The ammonia solution was then added drop wise to this trinary solution by continuous stirring until its attained the value of 3 in the pH scale and thereafter it drawn down to room temperature, and then cooled in ice bath. The resultant product was washed with cold water for several times to remove entire $Cl^-$ ion and dried with filter paper for 15 min before being transferred to drier at 100 °C for further drying. The obtained crude product was then recrystallised in hot methanol.

## 3 Characterization

Differential thermal analysis (DTA) and thermo gravimetry (TA Instruments-SDT Q600) of the prepared precursors were carried out from room temperature to 1,000 °C, with a heating rate of 20 °C min$^{-1}$ in dynamic air atmosphere. Fourier transform infrared spectroscopy (FT-IR) analysis (Thermo Nicolet Nexus 670) was undertaken to confirm the oxide and the residual organic moieties present in the sample. The X-ray diffraction (XRD) patterns of the co-precipitated nanopowders were measured by using a PANalytical—X′ pert pro diffractometer with Cu-Kα radiation ($\lambda = 0.15418$ nm) and a graphite monochrometer. The crystallite size $D$ of prepared powders was estimated using the Sherrer equation as follows [17].

$$D = 0.9\lambda/\beta\cos\theta \tag{1}$$

where $\lambda$, $\theta$, and $\beta$ are the X ray wavelength ($\lambda = 0.15418$ nm for Cu-Kα), Bragg diffraction angle, and the full width at half maximum of the diffraction peak (fwhm), respectively. The additional line broadening arising from micro strain causes the effect of distortion of the lattice plane and the imperfections in grain boundaries between crystallites. The distortion ratio was calculated using the formula [18].

$$(\beta)^2\cos^2\theta = \frac{4\lambda^2}{\pi^2 D} + 32\langle\varepsilon^2\rangle\sin^2\theta \tag{2}$$

where $\beta$ is the full width at half-maximum height of a diffraction peak at angle $\theta$, $D$ is the average particle size, $\langle\varepsilon^2\rangle$ is the crystal lattice distortion ratio. Furthermore, it is known that fwhm can be interpreted in terms of lattice strain and crystalline size [19] which can be expressed by the following equation.

$$\frac{\beta\cos\theta}{\lambda} = \frac{1}{\varepsilon} + \frac{\eta\sin\theta}{\lambda} \tag{3}$$

where $\varepsilon$ and $\eta$ are the effective particle size and the effective strain. The effective particle size taking strain into account can be estimated by plotting $\beta\cos\theta/\lambda$ versus $\sin\theta/\lambda$.

The resistivity was calculated for all antimony doped $SnO_2$ nanoparticles using the formula $\rho = RA/d$ where '$\rho$'is resistivity, $R$ is actual resistance, $A$ is the cross section area of circular pellet, and $d$ is the pellet thickness. The ATO nanopowders were pressed into a circular pellet of 7 mm diameter under 5 ton pressure for 2 min by using hydraulic pelletizer, and then putting this pellet between two rods of brass, its volume resistance by multimeter and its thickness by Vernier caliper were measured.

The chemical state of the elements in ATO particles was analyzed by XPS spectra using a Multilab 2000 X-ray Photoelectron spectroscope.

The Transmission electron micrograph (TEM) images were taken with FEI-Tecnai 20 G$^2$ transmission electron microscope. The samples for the TEM were prepared by ultrasonically dispersing the product in acetone, and then droplets were placed on carbon coated Cu grids.

## 4 Results and discussion

TG/DTA analysis was carried out to examine the conversion process of the precursors during calcinations. Figure 1 shows the profile of weight loss of precursor as a function of temperature, as measured by the TGA. The precursor precipitates showed a gradual weight loss between 30 and 500 °C, followed by a slow weight loss above 500 °C. The highest weight loss rate is observed around 100 °C. This highest rate is related with the release of water and chemisorbed methanol on the surface of the precursor. The DTA curve also showed gradual exothermic trend throughout the entire analysis range. This trend shows good correspondence with TGA data and means that precursor precipitates are transformed into oxide particles. After calcinations, ATO shows strong decrease of resistivity and color change from white to blue being attributed to the plasma absorption of the free conduction band electrons [16, 20, 21].
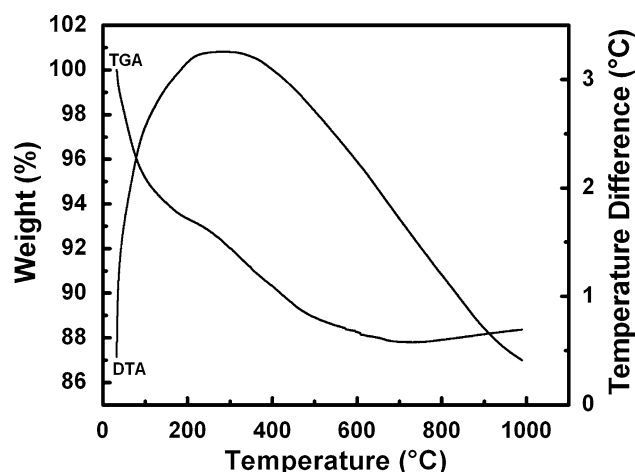
**Fig. 1** TG, DTA curves for the decomposition of ATO precursor at a heating rate of 20 °C min$^{-1}$ under a dynamic atmosphere of air

Figure 2 shows the FTIR spectrum of the antimony doped tin oxide nano powders prepared at room temperature and calcined to 500 °C for 4 h in air atmospheric condition by co-precipitation technique. From the Fig. 2a, it is observed that when calcinated at 500 °C sharp absorption peak at 592 cm$^{-1}$ in the finger print region is the characteristic vibration absorption of the Sn–O bond in SnO$_2$ [22] peak shifts to 631 cm$^{-1}$ which is assigned to the transverse $E_u$ modes of SnO$_2$. A very broadened absorption within 2,500–3,750 cm$^{-1}$ and sharp absorption band at 1,630 cm$^{-1}$ in the higher frequency region were also observed. The absorption peak found between 2,500 and 3,750 cm$^{-1}$ is assigned to O–H stretching from residual alcohol, water, and SnO–H bonds [23]. The sharp adsorption at 1,630 cm$^{-1}$ is associated with deformation vibration of H–O–H bonds of physisorbed water. Thus FTIR
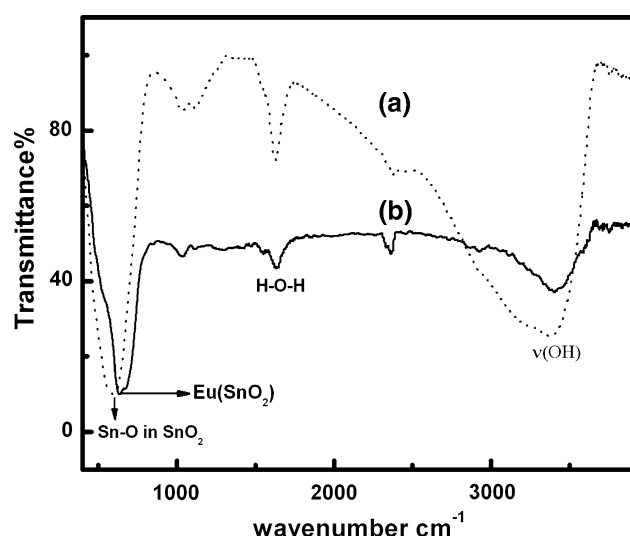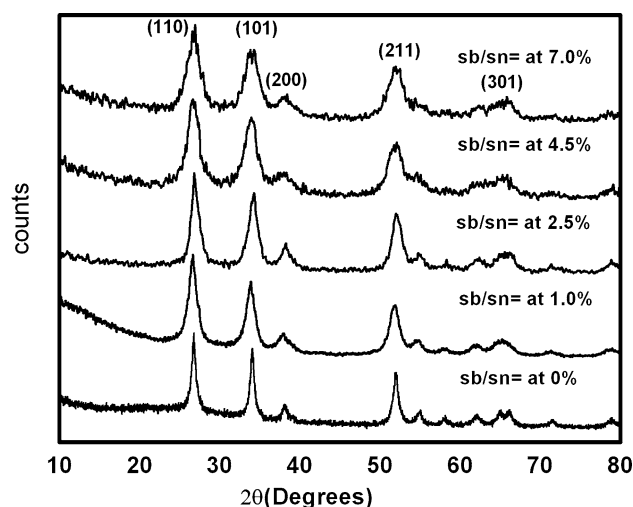
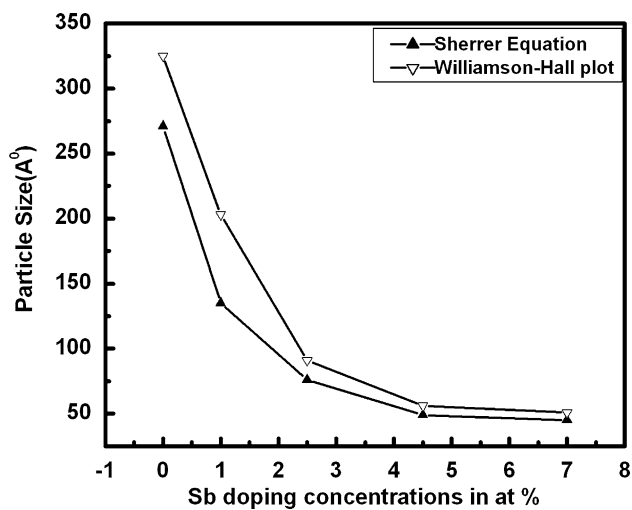spectrum confirms that some hydroxyl groups still remain, even in the samples calcined at 500 °C, as shown in Fig. 2b [24].

Figure 3 shows XRD patterns of the samples with different Sb doping concentrations calcined at 500 °C for 4 h in air atmospheric condition. All the diffraction lines are assigned well to tetragonal crystallites phases of antimony doped tin oxide with a reference pattern (JCPDS 882348). No phase ascribed to antimony compounds was detected indicating that all antimony ions might have come into the lattice of bulk SnO$_2$ for the substitute of tin ions [1]. The presence of broad peaks indicates the very small crystalline nature of ATO [2]. It is also found that the XRD peaks become gradually broadening with increasing Sb concentration, indicating the particles are reduced in size. The crystallite sizes determined from the Scherrer equation and Williamson–Hall plot are shown in Fig. 4. The reflection broadening in the XRD patterns attributed to the contributions of crystallite size, micro-strain and the instrument itself [3]. The line broadening arising from micro-strain causes the effect of distortion of the lattice plane and the imperfection of grain boundaries between crystallites.

Figure 5 shows the relationship between the different Sb doping concentration and the crystal lattice distortion ratio. When the concentration of Sb increases, the crystal lattice distortion ratio of the nanoparticles also increases .This could be explained in terms of increased crystal lattice distortion ratio when defect concentration rises. This may be attributed to the dopants Sb atoms distorting the SnO$_2$ crystal lattice.

Due to the presence of the crystal distortion in antimony doped tin oxide nanoparticles, lattice strain may be expected. The lattice strain may be calculated using Williamson–Hall plot. Figure 6a, shows the plot of $\beta \cos \theta / \lambda$



**Fig. 2** FT-IR spectra of Sb doped SnO$_2$; **a** as prepared powder and **b** calcined at 500 °C for 4 h in air atmospheric condition



**Fig. 3** XRD patterns of SnO$_2$ nanoparticles doped with different Sb concentrations
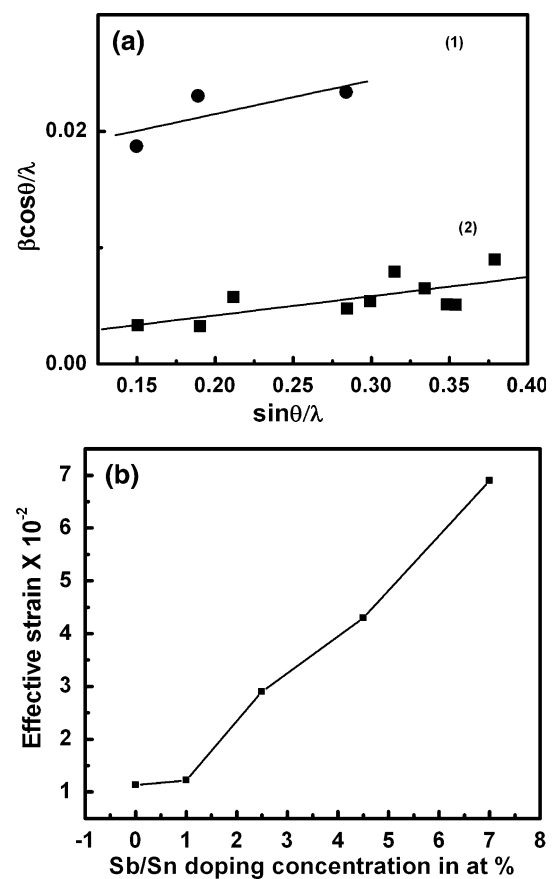
**Fig. 4** Different Sb doping concentration versus particle sizes were calculated using Scherrer and Williamson–Hall plot
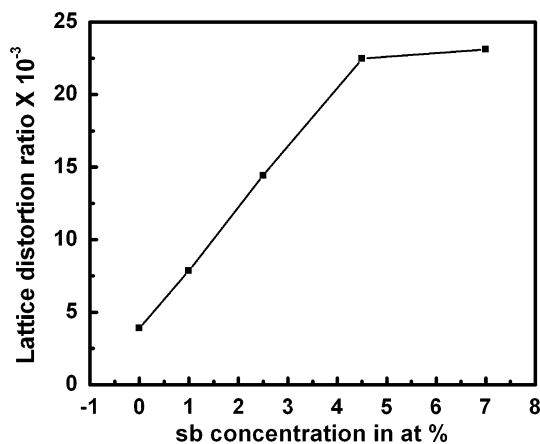


**Fig. 5** Shows different Sb/Sn doping concentrations with variation of lattice distortion ratio



**Fig. 6 a** Williamson–Hall plot of $SnO_2$ nanopowder doped with Sb; (1) Pure $SnO_2$ and (2) 7 at% Sb doped $SnO_2$ and **b** Variation of strain with Sb doping concentration

versus $\sin \theta/\lambda$ for pure $SnO_2$ and antimony (7 at%) doped $SnO_2$. In the representation $\beta$ is assumed to be the addition of line broadening due to micro-strain and due to particle size. Therefore, if we plot $\beta \cos \theta/\lambda$ versus $\sin \theta/\lambda$. Micro-strain is calculated from the slope and the particle size is obtained from the intercept. The Fig. 6b, shows the variation of strain with the concentration of dopants Sb in the $SnO_2$ matrix. Interestingly all prepared ATO nano particles having the positive slope attributing the presence of tensile strain. The higher magnitude of slope with the incorporation of Sb in $SnO_2$ matrix suggests the enhancement in the strain with the reduction in particle size.

Figure 7a, b illustrates TEM image and SAED pattern for antimony (7 at%) doped tin oxide nanoparticles. From Fig. 7a, it can be observed that the size of ATO particles falls in nano-scale, and these particles are almost agglomerated. Agglomeration of particles is a natural
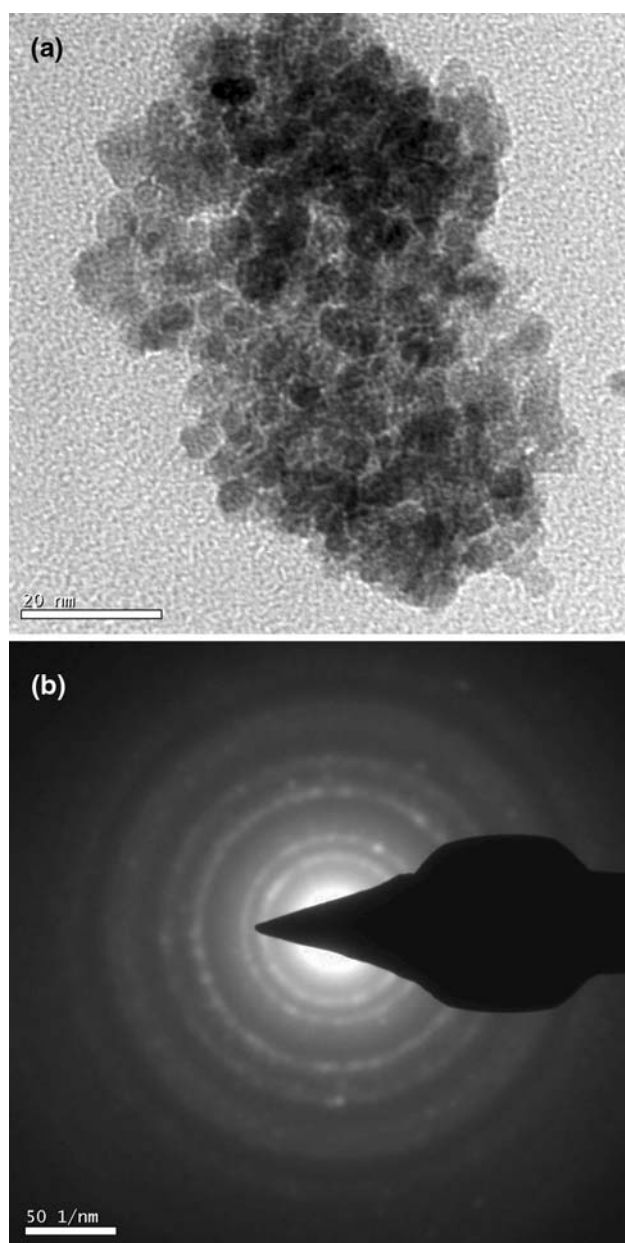
phenomenon. In the case of nanoparticles, agglomeration occurs very easily because the surface forces such as Vander-Waals forces, capillary forces and electrostatic forces can overcome only against gravitational and inertial forces for particles in this size range [25]. The average diameter of particles is evaluated to be approximately 5 nm. The results of grain size measurement from TEM observation are having good agreement to the X-ray line broadening method.

Antimony can have various oxidation numbers such as Sb(III), Sb(IV), and Sb(V) where only Sb(V) can play an electron donor role like the n-type semiconductor in the Sn(IV) lattice. Therefore, the electrical resistivity of the ATO powders is also related to the Oxidation number of Sb. If Sb(III) is also present in the Sb(V) doped Sn(IV) lattice, then Sb(III) will act as the electron acceptor and increases the resistivity. So, the XPS analysis was carried out to investigate the oxidation state of the Sb in the ATO powders prepared in this study.

The XPS narrow scan spectra of the ATO nanopowder (Sb = 7 at%) calcined at 500 °C for 4 h are shown in Fig. 8. The peak locations in all spectra were calibrated
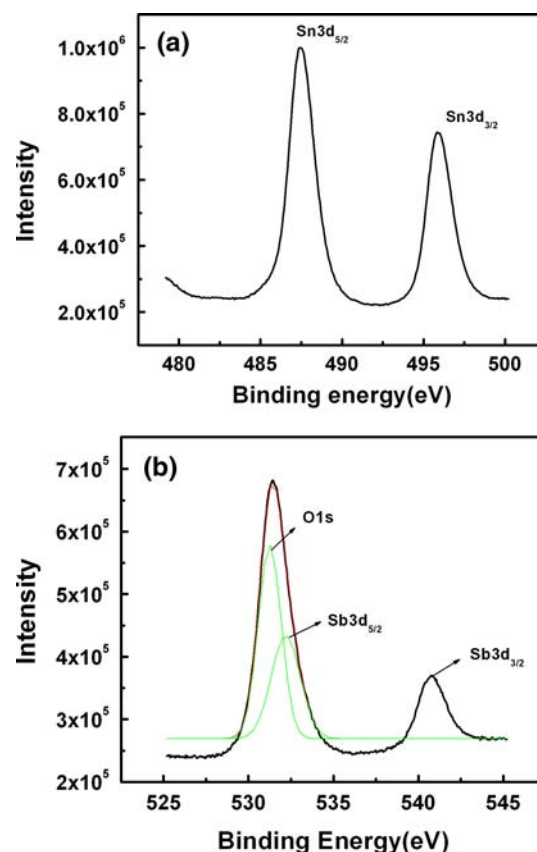
Fig. 7 **a** and **b** TEM image and SAED pattern of ATO (Sb = 7 at%) nano particles

donating one extra electron. This behavior is further confirmed through the electrical conductivity measurements.

The electrical resistivity was measured for the co-precipitated ATO nanopowders with various Sb doping contents as shown in Fig. 9. The resistivity value of the ATO nanopowders decreased with increasing antimony content and reached a minimum value of 4.7 $\Omega$ cm for the an antimony content of 7 at%. However, the ATO particle with the smallest particle size has the lowest resistivity value in this study. Therefore, it is suggested that the electrical resistivity of the ATO powders might be closely related to the ATO particle size and to the Sb ion concentration as well. The activation energy has been calculated and the values are found to be 0.096 and 0.0362 eV for $SnO_2$ and antimony (7 at%) doped SnO2, respectively. It may be recalled that in intrinsic $SnO_2$ the activation energy for electron transfer from valance band to conduction band must be around 3.6 eV [26]. Hence, the activation energy of 0.096 eV obtained for $SnO_2$ in the present study can be attributed to the transfer of electrons from defect/trap level present in $SnO_2$ to the conduction band. The decrease in activation energy and resistivity with antimony doping attributed mainly to the incorporation of

with the C1s (284.98 eV) as a standard reference. Image 'a' is the XPS spectra for Sn3d doublets. It can be seen that the binding energy of Sn3d5/2 and Sn3d3/2 is 487.46, 495.87 eV respectively. The gap between the Sn3d5/2 and Sn3d3/2 levels (8.41) is approximately as same as that of in the standard spectrum of Sn. The binding energy of Sn3d5/2 located at 487.46 shows the $Sn^{4+}$ bonding state from $SnO_2$. Image 'b' is resolved in to two peaks centered at 531.25 and 532.40 eV corresponding to O1s and Sb3d5/2. It indicates the presence of bonding O with $Sn^{4+}$ and $Sb^{5+}$. On calculating the relative peak area, presence of $Sb^{5+}$ dominates $Sb^{3+}$ that help to improve the conductivity by



Fig. 8 XPS spectra of the ATO nano powder calcined in air at 500 °C: **a** narrow scan of Sn3d; **b** narrow scan of Sb3d and O1s
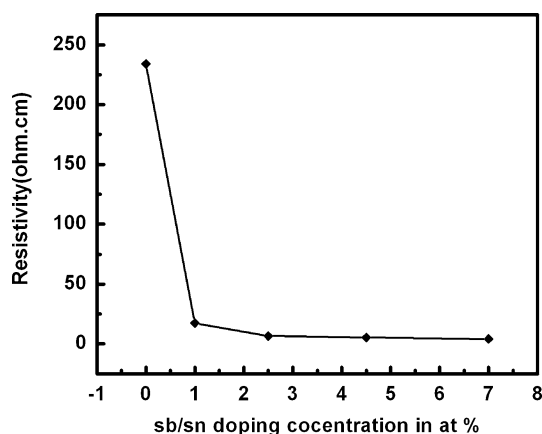
**Fig. 9** Different Sb doping concentration versus resistivity of ATO nano powders prepared by co-precipitation method

$Sb^{5+}$ ions in to $Sn^{4+}$ ion sites, which provides one extra carrier [27].

## 5 Conclusion

$SnO_2$ and Sb doped nano particle were prepared by co-precipitation technique. Oxide phase formation was confirmed through TG/DTA and FT-IR studies. X-ray diffraction pattern reveals that as prepared as particles are tetragonal structure. The particle size decreases with addition of the dopants and the strain contributes to line broadening were analyzed by the Williamson and Hall plot. Resistivity of the sample decreases with addition of the dopants. The activation energy were calculated using arrhenius equation for undoped $SnO_2$ and Sb doped $SnO_2$ which gives the values 0.096 and 0.0362 eV respectively, which is evident for the transfer of electrons from defect/trap level present in $SnO_2$ to the conduction band. Inclusion of $Sb^{5+}$ is confirmed through the XPS measurements. Nano particle nature of the prepared powder was established with TEM images.

## References

1. D.S. Ginley, C. Bright, MRS. Bull. **25**, 15–18 (2000)
2. T. Minami, Semicond. Sci. Technol. **20**, S35–S44 (2005)
3. R.B.H. Tahar, T. Ban, Y. Ohyaand, Y. Takahashi, J. Appl. Phys. **83**, 2631–2645 (1998)
4. S.J. Jeon, J.J. Lee, H.W. Kim, S.M. Koo, J. Ceramic Process. Res. **7**, 321–326 (2006)
5. T. Nutz, U. Felde, M. Haase, J. Chem. Phys. **110**, 12142–12150 (1999). doi:10.1063/1.479151
6. J. Zhang, L. Gao, Inorg. Chem. Commun. **7**, 91–93 (2004). doi:10.1016/j.inoche.2003.10.012
7. S. Shukla, L. Ludwig, C. Parrish, S. Seal, Sens. Actuators B Chem. **104**, 223–231 (2005). doi:10.1016/j.snb.2004.05.008
8. K. Sun, J. Liu, N.D. Browning, J. Catal. **205**, 266–277 (2002). doi:10.1006/jcat.2001.3456
9. J.J. Santos-Peña, T. Brousse, L. Sánchez, J. Morales, D.M. Schleich, J. Power Sources **97**, 232–234 (2001). doi:10.1016/S0378-7753(01)00620-6
10. J. Zhang, L. Gao, Mater. Res. Bull. **39**, 2249–2255 (2004). doi:10.1016/j.materresbull.2003.08.009
11. A.C. Bose, D. Kalpana, P. Thangadurai, S. Ramasamy, J. Power Sources **107**, 138–141 (2002). doi:10.1016/S0378-7753(01)00995-8
12. J. Zhang, L. Gao, Mater. Lett. **58**, 2730–2734 (2004). doi:10.1016/j.matlet.2004.01.041
13. W.M. Qiang, Z. QiYi, C. Ai, J. Chin. Ceram. Soc. **30**, 247–250 (2002)
14. K.C. Song, J.H. Kim, Powder Technol. **107**, 268–272 (2000). doi:10.1016/S0032-5910(99)00255-7
15. M.I.B. Bernardi, S. Cava, C.O.P. Santos, E.R. Leite, C.A. Paskocimas, E. Longo, J. Eur. Ceram. Soc. **22**, 2911–2919 (2002). doi:10.1016/S0955-2219(02)00057-2
16. J. Rockenberger, U. Felde, M. Tisher, L. Troger, M. Haase, H. Weller, J. Chem. Phys. **112**, 4296–4304 (2000). doi:10.1063/1.480975
17. B.D. Cullity, *Elements of x-ray diffractions* (Addison-Wesley, Reading, 1978), p. 102
18. S. Gao, L. Pang, H. Che, X. Zhou, China Particulogy **2**, 177–181 (2004). doi:10.1016/S1672-2515(07)60053-0
19. G.K. Williamson, W.H. Hall, Acta. metal. **1**, 22–31 (1953)
20. C. Kittel, *Introduction to solid state physics*, vol. 6 (Wiley, New York, 1986)
21. G. Boschloo, D. Fitzmaurice, J. Phys. Chem. B **103**, 3093–3098 (1999). doi:10.1021/jp9835566
22. S.T. Chang, I.C. Leu, M.H. Hon, Electrochem. Solid-State Lett. **5**, 71–74 (2002). doi:10.1149/1.1485808
23. M. Epifani, M. Alvisi, L. Mirenghi, G. Leo, P. Siciliano, L. Vasanelli, J. Am. Ceram. Soc. **84**, 48–54 (2001). doi:10.1111/j.1151-2916.2001.tb00606.x
24. V. Kersen, M.R. Sundberg, J. Electrochem. Soc. **150**, H129–H146 (2003). doi:10.1149/1.1570414
25. R.J. Pugh, L. Bergström, *Surface and colloid chemistry in advanced ceramic processing* (Marcel Dekker, New York, 1994), p. 273
26. C. Kilic, A. Zunger, Phys. Rev. Lett. **88**, 095501–095504 (2002). doi:10.1103/PhysRevLett.88.095501
27. C. Terrier, J.P. Chatelon, J.A. Roger, Thin Solid Films **295**, 95–100 (1997). doi:10.1016/S0040-6090(96)09324-8